Waves, Algebraic Growth, and Clumping in Sedimenting Disk Arrays

Rahul Chajwa,[1] Narayanan Menon,[2] Sriram Ramaswamy,[3] and Rama Govindarajan[1]
[1]*International Centre for Theoretical Sciences,*
Tata Institute of Fundamental Research, Bengaluru 560 089, India
[2]*Department of Physics, University of Massachusetts, Amherst, Massachusetts 01003, USA*
[3]*Centre for Condensed Matter Theory, Department of Physics,*
Indian Institute of Science, Bengaluru 560 012, India

(Received 12 February 2020; revised 3 August 2020; accepted 25 August 2020; published 22 October 2020)

An array of spheres descending slowly through a viscous fluid always clumps [J. M. Crowley, J. Fluid Mech. **45**, 151 (1971)]. We show that anisotropic particle shape qualitatively transforms this iconic instability of collective sedimentation. In experiment and theory on disks, aligned facing their neighbors in a horizontal one-dimensional lattice and settling at Reynolds number $\sim 10^{-4}$ in a quasi-two-dimensional slab geometry, we find that for large enough lattice spacing the coupling of disk orientation and translation rescues the array from the clumping instability. Despite the absence of inertia, the resulting dynamics displays the wavelike excitations of a mass-and-spring array, with a conserved "momentum" in the form of the collective tilt of the disks and an effective spring stiffness emerging from the viscous hydrodynamic interaction. However, the non-normal character of the dynamical matrix leads to algebraic growth of perturbations even in the linearly stable regime. Stability analysis demarcates a phase boundary in the plane of wave number and lattice spacing, separating the regimes of algebraically growing waves and clumping, in quantitative agreement with our experiments. Through the use of particle shape to suppress a classic sedimentation instability, our work uncovers an unexpected conservation law and hidden Hamiltonian dynamics which in turn open a window to the physics of transient growth of linearly stable modes.

DOI: 10.1103/PhysRevX.10.041016 Subject Areas: Fluid Dynamics, Soft Matter

I. INTRODUCTION

The collective settling of particles in viscous fluids is a classic and notoriously difficult problem in the physics of strongly interacting driven systems. In the Stokesian limit of Reynolds number $\mathrm{Re} \to 0$, inertia is negligible, viscous forces dominate, and a settling particle creates a flow field that decays slowly with distance r as $1/r$ [1–4]. Furthermore, particles in most natural and industrial settings are not spheres, and the hydrodynamics of settling couples their rotational and translational degrees of freedom [5–8]. The separation vector of two sedimenting spheres is constant [9,10], thanks to Stokesian time-reversal symmetry [11]. That of a pair of spheroids, in sharp contrast, is either time periodic or asymptotically diverging [12–14], an effect usefully understood through a surprising and precise analogy to Kepler orbits [15]. How particle anisotropy transfigures many-body sedimentation [16–19] is the central theme of this work.

The statistics of number fluctuations in sedimentation have been studied for collections of apolar [20–22] and polar [23] anisotropic particles in a steady state with spatially uniform mean concentration. Sedimenting lattices, on the other hand, break translation invariance and thus retain a reference microstructure [24] about which they display a rich dynamics [25–30] distinct from that of the uniform suspension. In addition, the presence of a lattice clarifies the connection between particle-level interactions and long-wavelength collective phenomena as seen in Crowley's celebrated clumping instability [25,26] of a regular array of sedimenting Stokesian spheres with purely hydrodynamic interactions. The Crowley instability can be understood by the composition of two-body interactions: (i) a trio of particles spaced slightly closer than the rest settles faster due to reduced drag $\mathbf{F}^D$; (ii) the resulting local tilt of the array leads to a lateral drift force $\mathbf{F}^{\mathrm{LC}}$, acting along the line joining their centers [2] [see Figs. 1(a) and 1(b)]. $\mathbf{F}^D$ and $\mathbf{F}^{\mathrm{LC}}$ together lead to dense regions breaking away from the array in clumps, on a scale given by the wavelength of the initial perturbation [see Video 1 in Supplemental Material (SM) [31]]. In this paper, we ask

---

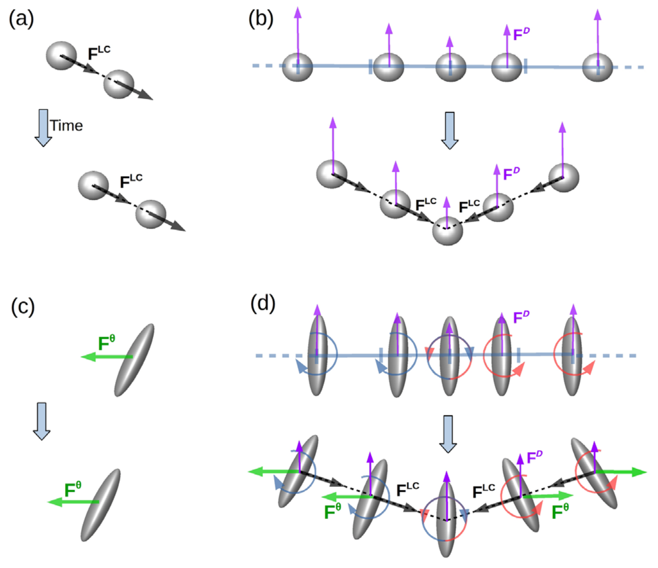

FIG. 1. Schematic of competing mechanisms. (a) F^{LC} acts on the pair along the line joining their centers leading to horizontal drift. (b) Clumping of array of spheres results from the line-of-centers force F^{LC}, acting along with reduced drag force F^D. (c) A spheroid drifts laterally as it falls when it is oriented obliquely with respect to gravity. (d) Lateral drift F^θ competing with the clumping induced by F^{LC} and F^D.

how nonspherical shape alters this central and inescapable feature of the sedimentation of sphere arrays.

We pursue this question experimentally and theoretically through the simple yet unexplored case of a freely sedimenting linear array of orientable apolar particles. Such a particle in isolation, aligned obliquely and settling under gravity, drifts laterally [see Fig. 1(c)] with a velocity that depends, for a given orientation, on the particle geometry through a mobility function [2] whose analytical form is known for spheroids [8,14]. When a collection of such particles settles in an array, the lateral drift $\mathbf{F}^\theta$ of an individual particle with tilt angle θ can compete with the line-of-centers force on a pair of particles $\mathbf{F}^{\mathrm{LC}}$, potentially preventing the clumping instability [see Fig. 1(d)]. We therefore ask, is a sedimenting lattice of oriented objects stable? We answer this question for a system of disks, that is, oblate spheroids with eccentricity $e \to 1$, as they display the most pronounced lateral drift [3,8,14]. We note further that, despite their ubiquity in nature, the sedimentation of disklike objects is much less studied than that of their rodlike counterparts [21,22], We show later that our findings can be generalized to all uniaxial apolar shapes.

In our experiments, we impose initial horizontal positional perturbations on a configuration in which the disks stand face to face, that is, each disk has its face normal aligned with the vectors joining it to its nearest neighbors, in a uniformly spaced horizontal array as depicted in Fig. 2(a). In the plane of perturbation wave number q and lattice spacing d, we find two distinct dynamical regimes—wavelike excitations with algebraic growth of perturbations, with no counterpart in sphere arrays, and linearly unstable modes—separated by a stability boundary. Crucially, the observed algebraic growth of perturbations occurs outside the regime of linear instability, in the neutrally stable regime. Using symmetries, we show that the long-wavelength dynamics of an array of uniaxial apolar objects, with the short dimension initially aligned horizontally, contains terms that compete with Crowley's [25] clumping instability.

Explicit construction of the dynamical equations of motion for Stokesian sedimenting spheroids, at the level of pair hydrodynamic interactions, determines the values of coefficients in our coarse-grained theory, and accounts for the experimentally observed instability boundary in the $q-d$ plane. In the neutrally stable regime we find an emergent elasticity which formally resembles that of a mass-and-spring chain, with the orientations of the disks playing the role of a momentum-density field which is conserved when summed over the entire lattice. The mode structure of the linearized nearest-neighbor theory, in the limit of thin disks, compares remarkably well with the experimentally measured frequency ω of the waves, wherein $\omega \to 0$ as wave number $q \to 0$. This "hydrodynamic" character of the modes is a dual consequence of translation invariance along x as a result of which only the relative x positions of the disks matter, and the apolar character of the disks, as a result of which there is no restoring torque if all disks are rotated through the same angle, and so the sum of all the angles acts like a conserved total momentum.

We observe transient algebraic growth of perturbations in the linearly stable regime in our experiments, and in the numerical solution of the far-field equations. We term this growth "nonmodal" since it occurs even when all modes of the dynamical matrix are neutral or decaying [32–35]. The underlying reason is that the dynamical matrix A is non-normal, i.e., $AA^\dagger \neq A^\dagger A$ (where the dagger represents the adjoint). Once the perturbation amplitude due to this nonmodal growth is large enough, nonlinearities can be triggered, disrupting the lattice through an unconventional route to instability at late times. Our calculations further predict the form of the initial perturbation that leads to maximum transient growth at each point in the neutrally stable regime in the q-d plane.

In following sections, we first show our experimental findings and rationalize them heuristically. Then we present a symmetry-based coarse-grained description, which is followed by the construction of the dynamical equations and their quantitative comparison with experimental observations.

II. EXPERIMENTS

Our experiments were conducted with disks of radius $a = 0.4$ cm and thickness 1 mm, 3D printed (FormLabs SLA) with stereolithography using resin of density 1.164 $\mathrm{g\,cm^{-3}}$, settling in silicone oil of density 0.98 $\mathrm{cm^{-3}}$ and kinematic viscosity 5000 cSt leading to a typical Reynolds number $\mathrm{Re} \sim 10^{-4}$. The particles are released in a one-dimensional array from the top of a quasi-two-dimensional glass container of width (x direction) $225a$, height (z direction) $112.5a$, and depth (y direction) $12.5a$. As shown in Fig. 2(a), the disks were initially placed with their surface normals $\mathbf{K}$ perpendicular to gravity and parallel to the line joining the disk centers. This was achieved by placing the disks in slots separated with a center-to-center spacing of $0.625a$ within a frame centered along the depth of the container. The clearance of each disk in its slot sets a precision of $0.0625a$ in the horizontal position, a deviation of up to 1.8° in orientation from the vertical, and negligibly small differences in initial vertical positions. Both the frame and the disks are already submerged in the fluid to suppress air bubbles that would otherwise affect sedimentation. The disks are then ejected from the slots at the same time with a comb whose teeth fit the slots in the array. The centers of the disks and their surface normals lie in the central (x, z) plane of the experimental geometry for much of their trajectory.

The reference state is an array of disks with uniform spacing achieved by choosing slots with separation d. On top of this initially uniform lattice, we impose horizontal positional perturbations $u_x(t = 0)$ at a wave number q by displacing disks appropriately to the right or left slot (see Fig. 7). The initial perturbations were measured to be sinusoidal with good accuracy, despite the discrete nature of the horizontal displacement. The clearance of the disks in the slots leads to random errors in initial orientations, which contributes to an error of $0.06a$ in imposed positional perturbation (see Fig. 8). Images were taken at 1/3 frames/s using a Nikon D750 D-SLR camera. The positions and orientations of the disks were tracked by fitting ellipses to every disk for each image frame. The centroid and angle of the ellipse give the center positions and orientation of the disks, respectively, with a precision of $0.02a$ and 0.5°. The time-dependent amplitude of the positional and orientation perturbation (u_x, u_z, θ) were measured by fitting a sine wave to the measured particle displacements and orientation relative to the reference lattice in the comoving frame.

III. TWO REGIMES OF DYNAMICS

As we vary lattice spacing d and perturbation wave vector q, we experimentally observe two distinct regimes of dynamics, as depicted in Figs. 2(b) and 3.

(i) *Waves of orientation coupled with number density fluctuations.*—For the initial condition in Fig. 2(b), we see that the disks at the density nodes hardly rotate, while the orientation and position of disks at the antinodes vary sinusoidally with time (see Fig. 7). Qualitatively, these wave dynamics may be explained by a composition of drag reduction, horizontal glide, and mutual rotation, as discussed in Fig. 1(d). Disks in regions of high number density fall faster than those in less dense regions due to reduced drag. The translational degree of freedom couples with rotations such that the disks in the dense region spread out due to orientational glide, stabilizing the lattice. This mechanism is characterized by change in sign of the rotation of disks at the antinodal points, which leads to waves (see Video 2 in SM [31]). This wave is eventually disrupted (see Video 3 in SM [31]), due to an amplification by nonmodal growth mechanism of the experimental imprecision in the initial orientation (see Fig. 8), as shown later in this article.

(ii) *Clumping instability decorated with orientations.*—A different type of dynamics is observed for the initial conditions in Fig. 3 where the perturbation quickly sharpens at the displacement nodes, or the high density regions. Just as in the Crowley instability of spheres, the dense regions fall faster due to reduced drag, and the vertical perturbation u_z increases. The orientation acts to spread out and rarefy the dense regions, but this effect is suppressed by the line-of-centers force leading to a clumping instability. The rotation of disks at the antinodal points does not change sign along the trajectory, in contrast with the wavelike regime. Figure 3(a) depicts a marginally unstable case where the initial horizontal perturbation neither grows nor decays substantially, whereas in Fig. 3(b) the horizontal perturbation grows to make the dense region more dense (see Videos 4 and 5 in SM [31]).

Later in the article, we show experimentally the regime of each of these two types of dynamics by varying initial conditions in the q-d space.

Theoretically, we go beyond this qualitative explanation at two levels. First, we understand our experimental observations using symmetries of the equations of motion for displacements and orientations, in the continuum limit of our system. Second, to determine the phenomenological coefficients in the symmetry-based equations for Stokesian sedimentation, we construct the dynamical equations of the lattice using pairwise addition of forces and torques resulting from the hydrodynamic interactions. We then show that the linearized dispersion relation of our theory compares quantitatively well with our experiments, while long time nonlinear instabilities can be understood by numerical investigations of the far-field equations of motion.

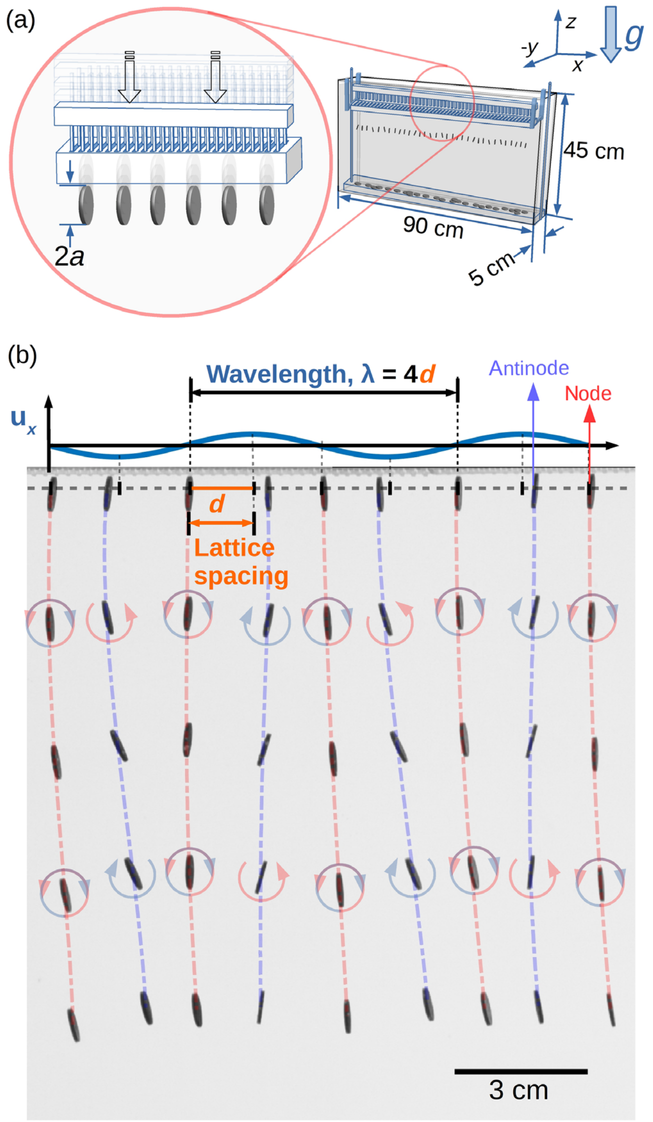

FIG. 2. (a) Schematic of the experimental setup. (b) Linearly stable mode. Overlapped time frames shown for time, $t = 0$, 130, 258, 386, 516 s. The unperturbed lattice of initial conditions is shown in gray dashed lines. Horizontal positional perturbation, u_x is sinusoidal with wavelength $\lambda = 4d$, lattice spacing of unperturbed state $d = 3.75a$, leads to undulations in orientation and vertical positions. The trajectories of disks at nodal and antinodal points are given by red and blue dashed lines, respectively. The rotations of disk orientations in clockwise and anticlockwise directions is given by blue and red circular arrows, respectively. The sense of rotation changes along antinodal trajectories (see Video 2 in SM [31]).

IV. SEDIMENTING SPHEROID LATTICE: SYMMETRY-BASED CONTINUUM THEORY

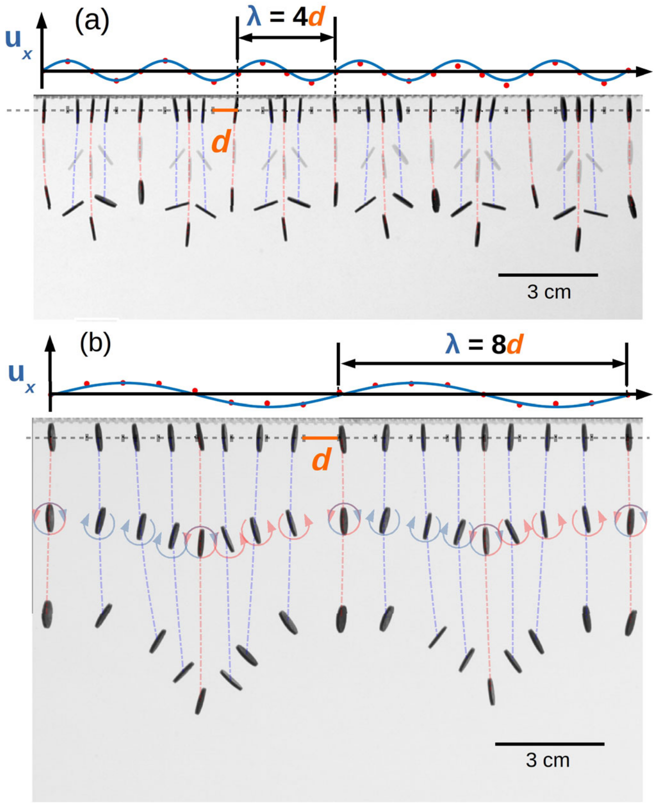

FIG. 3. Clumping instability. Overlapped frames (a) $t = 0$, 72, 135 s and (b) $t = 0$, 120, 255 s. In (a) initial horizontal perturbation wave number $q = 2\pi/\lambda = \pi/2d$ [same as Fig. 2(b)] and lattice spacing $d = 1.875a$ exhibit an unstable case, as line-of-centers force F^{LC} dominates over orientational drift F^{θ}. In (b) $d = 2.5a$ and $qd = \pi/4$ exhibits an unstable case leading to coarsening of the lattice followed by clumping in nonlinear regime. The trajectories of disks at nodal points are given by red dashed lines. Clockwise and counterclockwise rotation of disks, depicted as blue and red circular arrows, respectively, do not change color along the trajectory of the disks, in contrast with the wave shown in Fig. 2(b) (see Videos 4 and 5 in SM [31]).

We construct the hydrodynamic equations of motion of a drifting lattice of orientable objects, in the limit of no inertia, by writing the most general form of the mobility tensor (defined by velocity = mobility × force) allowed by the symmetries of the system, to leading order in a gradient expansion, extending theories [28,29] of the statistical dynamics of sedimenting crystals of pointlike objects. We find that the dynamical response of a lattice of orientable particles when perturbed about a suitable reference state contains terms that can compete with the clumping instability of isotropic particles [25,28]. We discuss the structure of the resulting wavelike modes.

The configurations of a periodic lattice of uniaxial objects are characterized, in a coarse-grained Eulerian description, by the displacement field $\mathbf{u}$ relative to the reference lattice and the orientation field $\mathbf{K}$ defined by the mean local alignment of the particle axes. For our geometry [see Fig. 4(a)] $\mathbf{K} = (\cos\theta, 0, \sin\theta)$, with θ equivalent to $\theta + \pi$ because the particles are fore-aft symmetric. The equations of motion for $\mathbf{u}$ and $\mathbf{K}$, in the presence of a gravitational driving force $\mathbf{F}$, must obey the following symmetries.

(i) Stokesian time-reversal symmetry under $t \to -t$ and $\mathbf{F} \to -\mathbf{F}$ [2].
(ii) translational invariance.
(iii) rotational invariance in the subspace perpendicular to gravity.
(iv) symmetry under inversion of orientations, $\mathbf{K} \to -\mathbf{K}$.

The mobility cannot depend directly on $\mathbf{u}$ due to translational invariance, but dependence on $\nabla\mathbf{u}$, $\mathbf{K}$, and $\nabla\mathbf{K}$ is allowed:

$$\frac{\partial \mathbf{u}}{\partial t} = \mathsf{M}(\nabla\mathbf{u}, \mathbf{K}, \nabla\mathbf{K}) \cdot \mathbf{F}, \tag{1}$$

$$\frac{\partial \mathbf{K}}{\partial t} = \mathsf{P} \cdot \mathsf{N}(\nabla\mathbf{u}, \mathbf{K}, \nabla\mathbf{K}) \cdot \mathbf{F}, \tag{2}$$

where M and N are the translational and rotational mobilities, respectively, and $\mathsf{P} \equiv \mathsf{I} - \mathbf{K}\mathbf{K}$ is the projector transverse to the unit vector $\mathbf{K}$. The other symmetries further constrain the allowed form of translational and rotational mobilities (see the Appendix B), leading, at lowest order in gradients, for a one-dimensional lattice along x, in a comoving frame, to

$$\frac{\partial u_x}{\partial t} = \lambda_1 \frac{\partial u_z}{\partial x} + \alpha K_x K_z, \tag{3}$$

$$\frac{\partial u_z}{\partial t} = \lambda_2 \frac{\partial u_x}{\partial x} + \beta K_z^2, \tag{4}$$

$$\frac{\partial K_z}{\partial t} = \gamma K_x \frac{\partial^2 u_x}{\partial x^2}. \tag{5}$$

Here, λ_i, α, and γ depend on $\mathbf{F}$ and the parameters governing the mobilities in Eqs. (1) and (2). Note that Eqs. (3)–(5) contain only hydrodynamic couplings proportional to the gravitational driving force, and our gradient expansion incorporates only local interparticle interactions. We have not included interactions arising from interparticle potentials or entropy. These enter at next order in gradients, and break Stokesian time reversibility [11].

Substituting $\mathbf{K} = (\cos\theta, 0, \sin\theta)$ in Eqs. (3)–(5) and linearizing about $\theta = 0$, the state where the particle axes are along x [Fig. 2(a)], leads, for disturbances with frequency ω and wave number q, to the dispersion relations

$$\omega_0 = 0, \qquad \omega_\pm = \pm q_x \sqrt{\lambda_1 \lambda_2 + \alpha\gamma}, \tag{6}$$

with elasticity contributing to Eqs. (5) and (6) at order q^2. For $\alpha \to 0$ the linearized equations for the translational degrees of freedom (u_x, u_z) are independent of $\mathbf{K}$ and reduce to those of the Lahiri-Ramaswamy model [28], with wavelike modes or an instability depending on the sign of $\lambda_1\lambda_2$ [28–30]. $\mathbf{u}$ affects $\mathbf{K}$ through the one-way coupling governed by γ. For $\alpha \neq 0$, translation and rotation are coupled, and the presence of $\alpha\gamma$ in the dispersion relation opens up the possibility of linearly stable wavelike dynamics even for $\lambda_1\lambda_2 < 0$. The linearized dynamics about the state where $\mathbf{K}$ is vertical corresponds to changing the sign of α in Eq. (6). For a system of sedimenting particles this means that the array is stable with either horizontal orientations or vertical orientations, but not both. Similar considerations arise in principle for the stability and dynamics [30] of driven flux lattices in thin slabs of type-II superconductors if the cross sections of the flux lines are noncircular.

V. SEDIMENTING SPHEROID LATTICE: PAIR HYDRODYNAMIC INTERACTIONS

We now go beyond symmetry considerations and explicitly construct the equations of motion for a settling lattice based on single-particle motion and addition of pairwise forces and torques at each particle position. We develop the theory for an array of spheroids, of eccentricity $e = \sqrt{1 - b^2/a^2}$, where a and b are the semimajor and semiminor axes, respectively. In the limit of $e \to 1$, an oblate spheroid approaches a disk shape, as in our experiments. We consider hydrodynamic interactions to leading order in a/r, where r is the separation between two particles. The ingredients of array dynamics are as follows.

(i) *Lateral drift of a single particle.*—An isolated settling spheroid cannot rotate, thanks to Stokesian time-reversal symmetry, but drifts horizontally with velocity

$$U_x^0 = \frac{F\alpha(e)}{12\pi\mu a} \sin 2\theta \tag{7}$$

[2,8], where F is its buoyant weight, μ is the dynamic viscosity of the fluid, and the mobility α is a function of the eccentricity. Figure 4(a) shows a schematic of a portion of our array, in which the orientation vector K^n of the nth particle is defined as a unit vector along the minor (major) axis for an oblate (prolate) spheroid. The angle θ^n is measured from the vertical as shown.

(ii) *Mutual drag reduction.*—Two particles at finite separation fall faster than an isolated one, due to the addition of the flow fields generated by each Stokes monopole [2,25]. In the far-field approximation, the increased vertical velocity to leading order in a/r is

$$U_z = -\frac{F}{6\pi\mu a} \frac{3a}{4r} \left[1 + \frac{(z_1 - z_2)^2}{r^2} \right]. \tag{8}$$

(iii) *Horizontal drift.*—The flow generated by the neighboring particle gives rise to a force along the line joining the centers of the two particles [2,25], which leads to a horizontal component of velocity,

$$U_x = -\frac{F}{6\pi\mu a} \frac{3a}{4r^3} (x_1 - x_2)(z_1 - z_2), \tag{9}$$

to leading order in a/r.

(iv) *Mutual rotational coupling.*—The presence of a neighboring particle generates a velocity field of nonzero vorticity, which to leading order in a/r gives a rotation

$$\dot{\theta} = F\frac{x_1 - x_2}{8\pi\mu r^3}. \qquad (10)$$

We proceed by combining ingredients (i)–(iv) to build the dynamics of the array of spheroids. We consider an infinite one-dimensional reference lattice along the x axis of uniformly spaced lattice points with spacing d and falling in the $-z$ direction. As shown in Fig. 4(a), we consider identical spheroids with orientation θ^n, and centroids at a small displacement (u_x^n, u_z^n) measured from each lattice point, where the superscript n stands for the nth particle. In the mean settling frame, pairwise addition of forces and torques on the nth particle due to hydrodynamic interactions with the $(n+l)$th and $(n-l)$th particles, for $l = 1, 2, 3, \ldots, \infty$, gives the equation of motion of the nth particle as

$$\frac{du_x^n}{dt} = -\frac{3a^2}{4d^2}\sum_{l=1}^{\infty}\frac{u_z^{n+1} - u_z^{n-1}}{l^2} + \frac{\alpha(e)}{2}\sin 2\theta^n, \qquad (11)$$

$$\frac{du_z^n}{dt} = +\frac{3a^2}{4d^2}\sum_{l=1}^{\infty}\frac{u_x^{n+l} - u_x^{n-l}}{l^2} + \alpha(e)\sin^2\theta^n, \qquad (12)$$

$$\frac{d\theta^n}{dt} = \frac{3a^3}{2d^3}\sum_{l=1}^{\infty}\frac{u_x^{n+l} + u_x^{n-l} - 2{u_x}^n}{l^3}. \qquad (13)$$

We have nondimensionalized the lengths and times using the semimajor axis a and the timescale $6\pi\mu a^2/F$, respectively, so that velocities are scaled by $F/6\pi\mu a$, the Stokes settling speed in the spherical limit. Setting $u_z^n = 0$ for all n in Eqs. (11) and (13) reveals that a sector of the dynamics can be written in terms of the canonically conjugate variables (u_x^n, θ^n) as

$$\dot{u}_x^n = \frac{\partial H}{\partial \theta^n}, \qquad \dot{\theta}^n = -\frac{\partial H}{\partial u_x^n}, \qquad (14)$$

with an effective Hamiltonian:

$$H = \frac{\alpha(e)}{4}\sum_m (1 - \cos 2\theta^m) + \frac{3a^3}{4d^3}\sum_{l,m}\frac{(u_x^m - u_x^{m+l})^2}{l^3}. \qquad (15)$$

The reduced dynamics under Eqs. (14) and (15) conserves both H and the total “momentum” $\sum_n \theta^n$. This Hamiltonian sector of the dynamics of our system extends the treatment of Ref. [15] to an array of disks. Effective Hamiltonians for Stokesian systems have also been presented for a swimmer in channel flow [36,37], the pair dynamics of bottom-heavy swimmers [38]—formally similar to Ref. [15], and, farther afield, driven rotor suspensions [39,40].

In the quasi-two-dimensional geometry of our experiments, bounded by closely spaced walls, truncating the interparticle hydrodynamic interaction at nearest neighbors so that particle n interacts only with particles $n \pm 1$, as in the treatment in [25], should be a good approximation. The Hamiltonian dynamics (14) and (15) of the settling array for $u_z = 0$, for small θ^n, becomes formally identical to that of the displacement and momentum-density fields, respectively, of a momentum-conserving monatomic mass-and-spring lattice. For fixed F the equations of motion are invariant under $t \to -t$, $u_x^n \to u_x^n$, $\theta^n \to -\theta^n$, $u_z^n \to -u_z^n$. A term in Eq. (13) of the form $\theta^{n+1} + \theta^{n-1} - 2\theta^n$, which within our analogy amounts to a momentum-conserving viscous damping, can arise if interdisk entropic or energetic aligning interactions, which break Stokesian time-reversal invariance, are taken into account. We do not pursue this issue further here except to note that within a linear stability analysis such a term would turn a neutral regime into a stable one.

Perturbing the angle about zero, $\theta = 0 + \delta\theta$, linearizing the equations, and Fourier transforming with respect to n gives the equation $\dot{\mathbf{X}}_q = \mathbf{A}(q)\mathbf{X}_q$, where $\mathbf{X}_q = (u_q^x, u_q^z, \delta\theta_q)$ is the spatial Fourier transform of the perturbations with wave number q along x, with dynamical matrix

$$\mathbf{A}(q) = \begin{pmatrix} 0 & -(3ia^2/2d^2)\sin q & \alpha(e) \\ +(3ia^2/2d^2)\sin q & 0 & 0 \\ -(6a^3/d^3)\sin^2 q/2 & 0 & 0 \end{pmatrix}, \qquad (16)$$

which is singular because in the linear approximation the dynamics of both u_q^z and $\delta\theta_q$ depend only on u_q^x. In Sec. VI we use the mass-and-spring analogy to define a natural inner product with respect to which we show that $\mathbf{A}(q)$ is non-normal, with physical consequences that we discuss in detail. Our treatment will be in the nearest-neighbor approximation, but the feature of non-normality can be seen to hold without this truncation. For now, we substitute the translational mobility function [3,8,14] for oblate spheroids, $\alpha(e) = [(9 - 6e^2)\tan^{-1}(e/\sqrt{1-e^2}) - 9e\sqrt{1-e^2}]/8e^3$, and for prolate spheroids, $\alpha(e) = \{(9 - 3e^2)\ln[(e+1)/(1-e)] - 18e\}/16e^3$, which gives the mode structure with two branches around $\omega = 0$ for each.

Oblate spheroids:

$$i\omega_{\pm}(q) = \pm\left|\sin\frac{q}{2}\right|\sqrt{\frac{3a^3}{4d^3e^3}(6e^2-9)\tan^{-1}\left(\frac{e}{\sqrt{1-e^2}}\right)+\frac{27a^3}{4d^3e^2}\sqrt{1-e^2}+\frac{9a^4}{2d^4}(1+\cos q)}. \tag{17}$$

Prolate spheroids:

$$i\omega_{\pm}(q,e) = \pm\left|\sin\frac{q}{2}\right|\sqrt{\frac{3a^3}{8d^3e^3}(3e^2-9)\ln\left(\frac{1+e}{1-e}\right)+\frac{27a^3}{4d^3e^2}+\frac{9a^4}{2d^4}(1+\cos q)}. \tag{18}$$

In the limit of $e \to 0$, the dispersion relations for both oblate (17) and prolate (18) spheroids converge to $i\omega_{\pm} = \pm(3a^2/2d^2)|\sin(q)|$, which is just the Crowley instability for spheres [25]. For $e \neq 0$, defining the nondimensional quantity $\tilde{d} \equiv 2d\alpha(e)/3a$ gives a universal condition for stability:

$$\tilde{d} \geq \cos^2\frac{q}{2}, \tag{19}$$

so that $\tilde{d} = \cos^2 q/2$ defines the stability boundary in the $\tilde{d} - q$ plane, separating the regime of kinematic waves (blue) from the clumping instability (red) as shown in the phase diagram of Fig. 4(b). In general, for a uniaxial apolar shape, α is a constant parameter [2] which can be determined by experimentally measuring the lateral drift of an isolated settling object. From Eq. (16) it follows that our expression for the stability boundary (19) applies to all axisymmetric apolar shapes, when d is rescaled by $2\alpha/3a$.

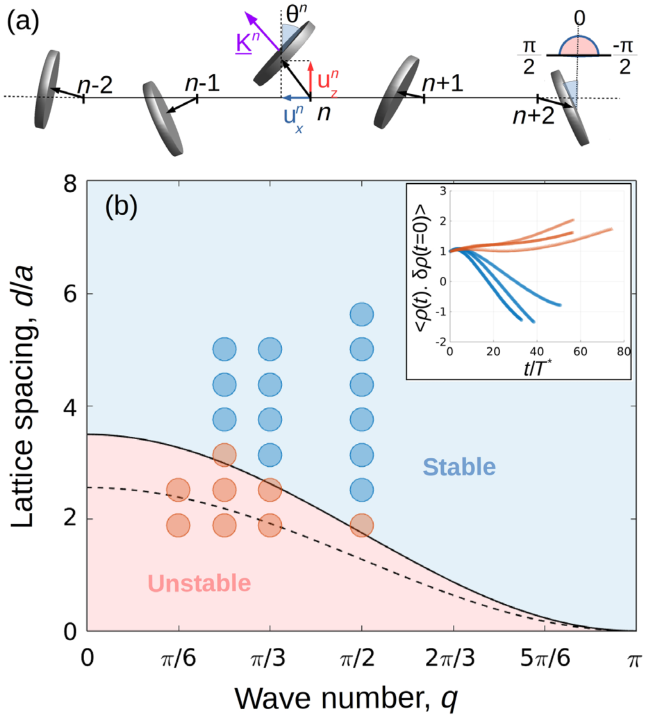

FIG. 4. Phase diagram. (a) A schematic of the array of disks showing spatial perturbations (u_x^n, u_z^n) and orientation perturbation θ^n of the nth disk which interacts hydrodynamically with the neighbors $n-i$, $i = 1, 2, \ldots$. For prolate spheroids the orientation vector $\mathbf{K}^n$ is rotated by $\pi/2$ from the one shown. (b) The phase diagram with the stable regime shown in blue and unstable regime in red. The experimental data points (circles) are colored blue or red by measuring whether the density autocorrelation grows or decays, which is shown in the inset of (b), for some representative stable (blue) and unstable (red) points in the q–d plane, where timescale $T^* = \mu d^2/F$. The phase boundary predicted by the linear theory with nearest-neighbor interaction is shown for oblate spheroids with eccentricity approximating the experimental thickness, $e = 0.9922$ (solid line) and spheroid of zero thickness $e = 1$ (dashed line).

This prediction agrees well with our experimental data shown by the red and blue circles, where we have initialized the lattice at those points in the $\tilde{d}$-q plane. The outcome of any given experiment is identified as being wavelike or clumping by considering the early stages of the time dependence of $\langle\rho(t)\delta\rho(t=0)\rangle$, normalized amplitude of the density autocorrelation, which is measured by projecting the particle number density $\rho(t) = \sum_{m=1}^{N}\delta(x - x_m(t))/N$, on the initial density fluctuation $\delta\rho(t=0)$ of the lattice. We obtained $\delta\rho(t=0)$ by fitting a sine to the initial horizontal displacement perturbation $u_x(t=0)$, and shifting in phase by $\pi/2$. This is shown in the inset of Fig. 4(b), where some curves increase in amplitude and others decay. At later times, even in the wavelike regime, the perturbation becomes very nonsinusoidal, as nonlinear effects become prominent.

More specifically, the limit of disks with zero thickness ($e \to 1$ for oblate spheroids) produces the mode structure shown in Fig. 5(a):

$$i\omega_{\pm}(q) = \pm\frac{3a^2}{2d^2}\left|\sin\frac{q}{2}\right|\sqrt{\left(-\frac{d\pi}{2a}+4\cos^2\frac{q}{2}\right)}, \tag{20}$$

which produces neutrally stable modes when the lattice spacing $d > 8a\cos^2(q/2)/\pi$ and clumping instability otherwise. This prediction is compared with experimental data for the frequency in Fig. 5(b) for various q and d. We show solutions corresponding both to zero thickness as well as for the ellipsoid with $2a$ and $2b$ corresponding to

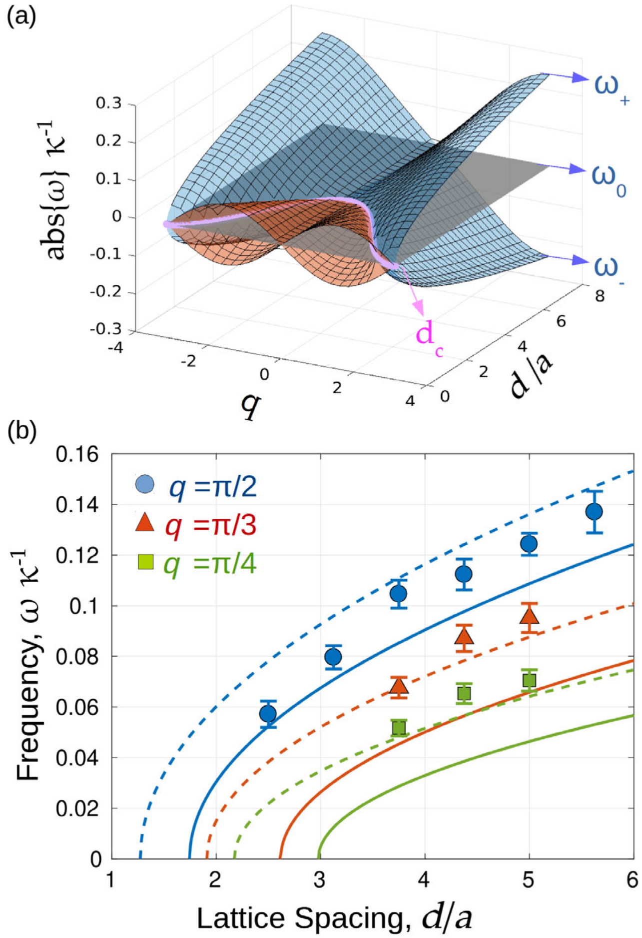

FIG. 5. Spectrum. (a) The branches of the spectrum. The absolute value of the complex frequency scaled by $\kappa = 6\pi a^2/d^2$ is shown as a function of the nondimensional wave number q and spacing d. The blue surface is for purely real frequencies (the neutrally stable modes) and the red surface is for purely imaginary frequencies (clumping instability). The boundary between the stable and unstable regimes is shown by the magenta curve d_c. (b) Measured nondimensional frequency $\omega\kappa^{-1}$ (symbols) for various wave numbers q plotted against the lattice spacing d/a. The curves are predicted by our nearest-neighbor theory for oblate spheroids, solid lines for the experimental eccentricity $e = 0.9922$, and dashed lines for the limit of zero thickness $e = 1$.

the diameter and thickness of our disks. In the long-wavelength limit $q \to 0$, Eq. (20) reduces to the dispersion relation (6) predicted using symmetry arguments in the previous section. The phenomenological coefficients in Eqs. (3)–(5) are thus determined for disks to be $\lambda_1\lambda_2 = -9a^4/4d^4$ and $\alpha\gamma = 9\pi a^3/32d^3$.

The limit for needles of zero thickness (prolate spheroids with $e \to 1$) is not well defined, but the dispersion relation for rods of small thickness $2b$ and length $2a$, to leading order in $1 - e$, is

$$i\omega_\pm(q) = \pm\frac{3a^2}{2d^2}\left|\sin\frac{q}{2}\right|\sqrt{\frac{3d}{a}-\frac{2d}{a}\ln\left(\frac{2a}{b}\right)+2\cos^2\frac{q}{2}}. \quad (21)$$

Note that the gapless feature ($\omega \to 0$ as $q \to 0$) of the modes (17) and (18) is tied to the conservation of total "momentum" $\sum_n \theta^n$ and the breaking of continuous translational symmetry by the lattice. Although the lattice was not formed by a phase transition to an ordered state, our imposition of an array structure on a translation-invariant background means that only the relative positions of disks matter, so the displacement field behaves like a true broken-symmetry mode [41].

VI. NON-NORMALITY AND THE TRANSIENT ALGEBRAIC GROWTH OF WAVELIKE MODES

We show below that the dynamical matrix $\mathbf{A}(q)$ of Eq. (16) is non-normal with respect to a natural inner product. This feature can [33,34]—and in the present case does—lead to short-time behavior quite different from what one might expect naively from the exponential evolution of the eigenmodes. In particular, even when all the eigenvalues show negative or zero growth rate, disturbances can grow algebraically for some time [35]. The amount of growth depends on both the operator and on the configuration of the initial perturbation. For small growth, the system will relax at large times to the behavior expected from the least stable eigenmode. When the transient growth is significant, however, the system is ultimately pushed into the nonlinear regime. In hydrodynamic stability problems, especially in shear flows [42], transition to turbulence through the algebraic growth route is quite common. However, experimental quantification of algebraic growth is extremely difficult. The present work offers a rare quantitative comparison of transient growth in theory and experiment.

For disks, the eigenfunctions of the dynamical matrix (16) can be used to construct the solution for experimental initial conditions. The eigenvectors corresponding to the eigenvalues $(0, i\omega_-, i\omega_+)$ defined in Eq. (20) are respectively given by the columns of the matrix:

$$\begin{pmatrix} 0 & i\omega\pi\csc^2\left(\frac{q}{2}\right) & -i\omega\pi\csc^2\left(\frac{q}{2}\right) \\ -i\frac{d\pi}{8a}\csc(q) & -\frac{1}{2}i\cot\left(\frac{q}{2}\right) & -\frac{1}{2}i\cot\left(\frac{q}{2}\right) \\ 1 & 1 & 1 \end{pmatrix}. \quad (22)$$

The experimental initial perturbation $(u_x, u_z, \delta\theta) = (\epsilon, 0, 0)$ in the neutrally stable regime gives waves of displacement and orientations (see Appendix C):

$$u_x^n(t) = \epsilon\sin(qn)\cos(\omega t), \quad (23)$$

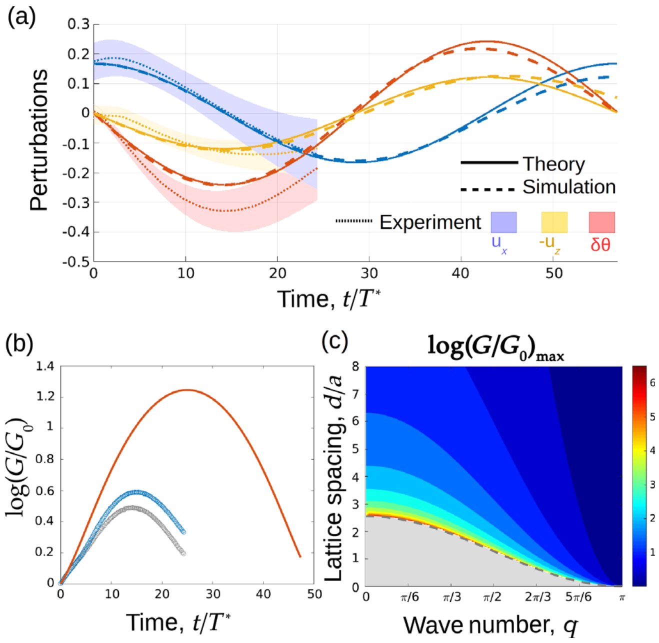

FIG. 6. Nonmodal growth. (a) The experimental amplitude for the angle (red patch), horizontal perturbation (blue patch), and vertical perturbation (yellow patch) compared against theory (solid lines) and far-field simulation of oblate spheroids in limit of zero thickness (dashed lines), for the stable case of $q = \pi/2$ and $d/a = 3.75$, with spatial perturbations and time nondimensionalized by d and $T^* = \mu d^2/F$, respectively. The extent of the shaded region shows the corresponding error in measurement of amplitude. (b) The nonmodal growth plotted for the stable case $q = \pi/2$ and $d/a = 3.75$ (blue) and energy of the analogous mass-and-spring lattice (gray) in experiments, compared with the simulation for the initial condition that gives maximum gain (red) in $t = 14T^*$, where G_0 is the initial amplitude. (c) The log of ratio G/G_0, of maximum amplitude G of the nonmodal perturbation to the initial amplitude G_0 depicted for the neutrally stable regime in the $q - d/a$ plane.

$$u_z^n(t) = \frac{\epsilon \sin(q)}{4\omega\pi} \cos(qn) \sin(\omega t), \tag{24}$$

$$\delta\theta^n(t) = -\frac{\epsilon \sin^2(q/2)}{\omega\pi} \sin(qn) \sin(\omega t). \tag{25}$$

The time dependence predicted here is in good agreement with the experimental data shown in Fig. 6(a) for $q = \pi/2$ and $d/a = 3.75$. This result is also compared to the numerical integration of the far-field equations with periodic boundary conditions (as discussed in Appendix D), remaining in the limit of small a/d but retaining nonlinearities to one further order in u/r than in Eqs. (7)–(10) (see Video 6 in SM [31]).

The appropriate definition of an inner product is not far to seek. We see from Eq. (15) that the dynamics in the absence of u_q^z, linearized in θ^n and truncated at nearest neighbors, is precisely that of a chain of particles with mass $1/\alpha(e)$ connected by Hookean springs with stiffness $3a^3/2d^3$. It is convenient to work with rescaled variables $\tilde{\mathbf{X}}_q \equiv [U_q, W_q, \Theta_q]^T = [\sqrt{3a^3/d^3}\sin(q/2)u_q^x, \sqrt{3a^3/d^3}\sin(q/2)u_q^z, \sqrt{\alpha(e)/2}\theta_q]^T$, in terms of which the dynamics reads $d\tilde{\mathbf{X}}_q/dt = \sqrt{6\alpha(e)a^3/d^3}\sin(q/2)\tilde{\mathbf{A}}(q)\tilde{\mathbf{X}}_q$, with

$$\tilde{\mathbf{A}}(q) = \begin{bmatrix} 0 & -i\lambda & 1 \\ i\lambda & 0 & 0 \\ -1 & 0 & 0 \end{bmatrix} = \begin{bmatrix} 0 & -i\lambda & 0 \\ i\lambda & 0 & 0 \\ 0 & 0 & 0 \end{bmatrix} + \begin{bmatrix} 0 & 0 & 1 \\ 0 & 0 & 0 \\ -1 & 0 & 0 \end{bmatrix}, \tag{26}$$

with $\lambda = \sqrt{3a/2d\alpha(e)}\cos q/2$. For perturbations with $W_q = 0$, the dynamics implied by Eq. (26) conserves $|U_q|^2 + |\Theta_q|^2$, which is simply the energy for the Hamiltonian part of the dynamics via Eqs. (14) and (15). The Euclidean norm $|U_q|^2 + |W_q|^2 + |\Theta_q|^2$ is then a physically reasonable measure of size for vectors with a nonzero W component as well, and the Hermitian conjugate of an operator then takes the familiar form of the complex conjugate of its matrix transpose. From Eq. (26), $\tilde{\mathbf{A}}(q)$ can be seen to be the sum of a Hermitian operator for the unstable Crowley [25] dynamics of U_q and W_q and a skew-Hermitian (in fact real-antisymmetric) operator for the coupled dynamics of U_q and Θ_q. Each is normal, but the two do not commute with each other, and hence $[\tilde{\mathbf{A}}(q), \tilde{\mathbf{A}}^\dagger(q)] \neq 0$, i.e., $\tilde{\mathbf{A}}(q)$ is non-normal.

The equations for $\tilde{\mathbf{X}}_q$ (26) imply that the rate of change of the effective energy is

$$\frac{d}{dt}\langle \tilde{\mathbf{X}}_q | \tilde{\mathbf{X}}_q \rangle = 6\frac{a^2}{d^2}\sin q \,\mathrm{Im}(U_q^* W_q), \tag{27}$$

whence we see that the perturbation can grow for suitable initial choices of U_q and W_q, i.e., u_q^x and u_q^z. The "vibrational modes" contribution $U_q^* U_q + \Theta_q^* \Theta_q$ is precisely half of the total in Eq. (27). Despite the absence of an eigenvalue with positive real part, non-normality allows the destabilizing coupling between u_q^x and u_q^z to infect the dynamics in the form of transient algebraic growth of perturbations or effective energy even in the "stable" regime of the phase diagram [see Fig. 6(b)]. If the transient amplitude is large enough, nonlinear growth takes over, as in our experiment. In our far-field numerical solution, on the other hand, we have the facility to reduce the initial amplitude so much that despite transient growth the system remains linear.

To quantify the nonmodal growth in the q-d plane, we calculate the norm of $\exp(\tilde{\mathbf{A}}s)$ for all times s, and calculate the maximum amplitude $G_{\max}$ attained by the perturbation over all s, which is finite in the stable regime and depends on wave number q and lattice spacing d [see Fig. 6(c)]. For each point in the (q, d) plane we can predict the initial perturbation which gives the maximum nonmodal growth at time s from singular value decomposition of $\exp(\tilde{\mathbf{A}} * s)$

at that point. This initial condition is given by the first column of the right-singular matrix of $\exp(\tilde{\mathbf{A}} * s)$. The growth of this maximally growing initial lattice configuration is compared against the experimental perturbation using far-field simulation of oblate spheroids in the limit of disk $e \to 1$ [see Fig. 6(b)]. Further, our numerical study of the far-field equations (see Appendix D) shows that the observed disruption of the lattice in the stable regime results from amplification of the experimental noise in the initial orientations (see Videos 3 and 7 in SM [31]).

We see thus that even in the regime where the orientational degree of freedom defeats the Crowley mechanism, and linear stability predicts waves, transient growth ultimately triumphs. An array of sedimenting spheroids is thus disrupted at all q and d. In our numerical study with periodic boundary conditions we are able to observe the waves and delay the onset of nonlinearity by reducing the amplitude of the initial perturbations, unlike in the experiments where there are inevitable imprecisions in the initial conditions.

VII. CONCLUSIONS

The many-body physics of collective sedimentation holds many challenges and provokes many debates [16,19], which we must consider anew if we are to understand the role of internal degrees of freedom arising from particle shape. We study the role of particle orientation in the minimal setting of a one-dimensional lattice of Stokesian settling disks, and show the existence of two regimes of dynamical behavior, as a function of lattice spacing and perturbation wave number. One of these is an extension of Crowley's clumping instability [25] to nonspherical particles. The second is a hitherto unknown state of orientation and displacement waves, where the drift and mutual interaction of the disks overcome the clumping instability. We thus identify an unexpected mechanism to resist instabilities that were identified for spheres 50 years ago [25], were elaborated into parallel ideas about spheroids in a landmark paper 30 years ago [20], and opened new directions in nonequilibrium statistical mechanics 20 years ago [28]. This competition between orientation and clumping in spheroids is related to an effect predicted for polar (self-aligning) particles [23], but our mechanism is crucially distinct from theirs due to different particle symmetries. In particular, orientation is not a slow variable for polar particles and thus does not enter in the "hydrodynamic" equations. In contrast, our disks rotate dynamically, thanks to apolarity and the local interparticle interactions in the form of a coupling (10) which arises from the antisymmetric part of the local fluid velocity gradient. The importance of these ingredients in our collective dynamics suggests a possible new consideration to be included in the statistical theory of Koch and Shaqfeh [20].

The wavelike regime is unusual in that we predict, and observe experimentally, large transient growth that ultimately destabilizes the lattice, through nonlinear effects arising from the amplification of initial experimental error in release. Thus, the lattice is nonlinearly unstable over the entire q-d plane, but due to two very different mechanisms. This unusual mechanism for nonlinear instability, namely, transient algebraic growth of perturbations in a linearly stable regime, should be of relevance in many other dissipative dynamical systems, but is not widely known, as not many examples have been identified and studied in the laboratory. We hope our experimental findings and theory will stimulate others to seek this mechanism in systems where the cause of long-term instability is ascribed to unidentified drifts or noise sources. In our system (26) non-normal time evolution originates from noncommutativity between two separately normal parts of the dynamics: that of particle positions alone, and that of orientations coupled to positions. The distinct character of these two contributions is a generic feature of Stokesian hydrodynamic interaction with orientational degrees of freedom. Therefore, algebraic growth is also expected in any future studies of higher-dimensional lattices of oriented objects. The fact that our calculation, and the accompanying numerics, allows us to capture both the mode structure and the growth of perturbation amplitude reassures us that our numerical model can in the future be used to gain a comprehensive understanding of the unstable regime and of other lattice configurations.

Further, we show that the momentumlike character of the particle orientation, seen earlier in a pair of settling disks [15], plays a crucial role in the collective dynamics of the disk array. The conservation of total momentum, in conjunction with broken continuous translational invariance, yields gapless modes ($\omega \to 0$ as $q \to 0$) in this spatially extended driven dissipative system. An important characteristic of the system we studied is that there is no evolution of the angles when disks are globally rotated. This is related to the orientation independence of the gravitational energy of *apolar* shapes, but is ultimately a consequence of Stokesian time reversibility. Objects with *polar* shape will have a preferred orientation in a gravitational field [6,43,44], hence a damping of the momentum corresponding to $\sum_n \theta^n$, at zero wave number in Eq. (13), and therefore an overdamping of the wavelike modes at small wave number.

The dynamics of sedimenting lattices of particles with more complex shapes that are polar or chiral [45,46] remains open to investigation and is expected to show behaviors distinct from the apolar shapes discussed here. Finally, sedimenting objects in the natural world, like flakes of clay particles in river beds or red blood cells settling in plasma, are disklike [47,48], and we believe our work offers a useful building block to understand the role of particle shape in these complex fluid-mechanical phenomena.

ACKNOWLEDGMENTS

R. C. and R. G. acknowledge support of the Department of Atomic Energy, Government of India, under Project No. 12-R&D-TFR-5.10-1100. S. R. was supported by a J. C. Bose Fellowship of the SERB (India) and by the Tata Education and Development Trust, and acknowledges support from an Adjunct Professorship with TIFR. N. M. was supported through NSF DMR 1905698.

APPENDIX A: EXPERIMENTAL METHODS

1. Initial perturbations

The control parameters in experiments are the lattice spacing of the reference lattice and wavelength of the initial horizontal positional perturbation around this reference state. This was achieved using 3D printed stacks of rectangular slots of width 0.125 cm and height 0.90 cm, with disks of thickness 0.1 cm and diameter 0.8 arranged in a periodic pattern initially as shown in Fig. 7. This perturbation was made as close to sinusoidal as possible within the constraint of discretization imposed by the slots (see Fig. 7). After arranging the disks across the total length of the release mechanism of 80 cm, the disks were poked out gently while the whole mechanism was submerged roughly 3 cm below the surface of the fluid, to avoid any bubbles. After the disks were released out of the slots, they were measured to have a random orientation error sitting on the spatial perturbation which we imposed (see Fig. 8). This angular error corresponds to an error in horizontal spatial perturbation in u_x of ± 0.03 cm. This error in release plays a crucial role in disrupting the lattice at late times in the linearly stable, but transiently growing, regime.

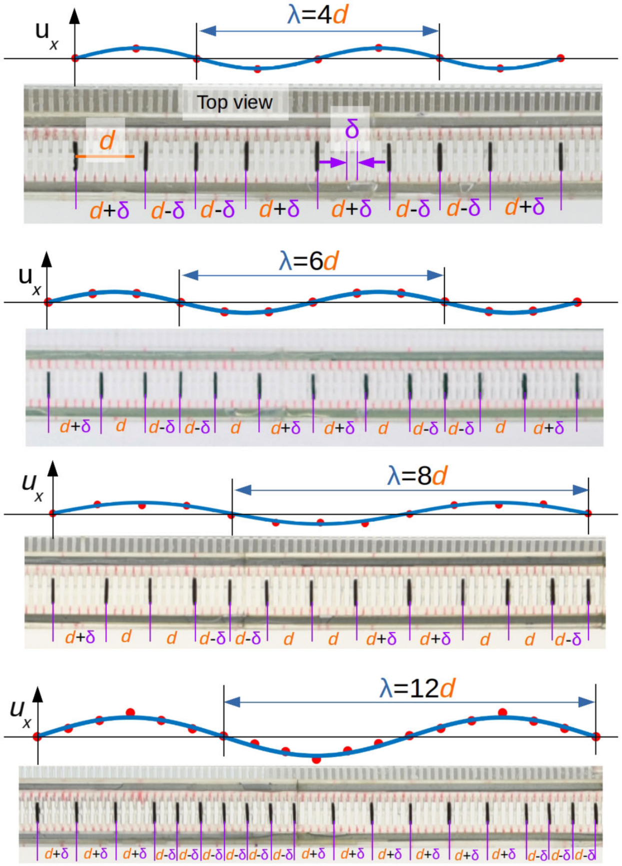

FIG. 7. Release mechanism. Top view of the release mechanism shown before release, with the disks loaded in the slots. The center-to-center distance between adjacent slots is δ and the lattice spacing of reference lattice is d. Initial horizontal positional perturbations u_x are shown by fitting a sine function (blue curve) to the measured perturbations (red dots) for the wavelengths $\lambda = 4d$, $6d$, $8d$, and $12d$.

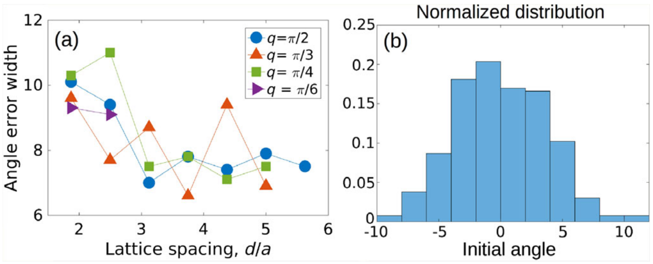

FIG. 8. Error in initial orientation. (a) The error is quantified by 0.5(maximum-minimum) of the initial angles in any given run. This measure of the width in release angle is plotted here as a function of lattice spacing for $qd = \pi/2, \pi/3, \pi/4$, and $\pi/6$. (b) A combined distribution of initial angles of several experimental runs for a fixed $qd = \pi/2$ and $d = 3.75a$.

2. Measuring frequency

The wave nature is evident in the dynamics of the orientations and positional perturbations which exhibit a quarter cycle of the wave with reasonable accuracy, before the nonlinear instabilities kick in via an algebraic growth of perturbations, in contrast with the exponential growth of perturbations in the unstable regime. The positions and orientations of the disks are measured at each frame every 3 s by fitting an ellipse around each disk. The reference lattice is constructed by measuring the largest node-to-node

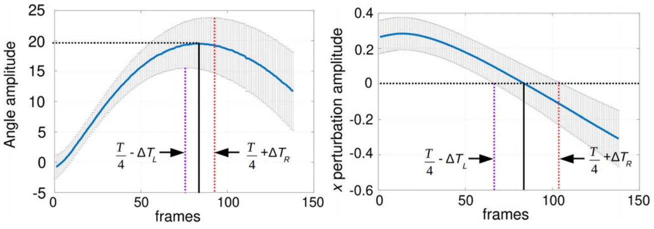

FIG. 9. Frequency measurement. Amplitude of the fitted sine wave plotted for the angle and the horizontal positional perturbations, along with the residual error of the fit shown as vertical error bar at each frame. At quarter time period of the wave, the amplitude of angle peaks and the horizontal perturbation crosses $y = 0$ axis, consistent with our theory.

distance in the initial condition. It is assumed that this reference lattice settles down vertically with the mean settling speed of the lattice and the orientation and positional perturbations are measured for the particles corresponding to each lattice point. A sine wave is fitted in the perturbation with specified wave number at each frame and the amplitude of the fitted wave is measured at each time step (see Fig. 9). The residual of this fit gives error in frequency measurements as the amplitude for u_x and θ is plotted as a function of time.

APPENDIX B: CONSTRUCTING MOBILITY USING SYMMETRIES

The gradient expansion of the translational mobility $\mathsf{M}(\nabla\mathbf{u}, \mathbf{K}, \nabla\mathbf{K})$ and rotational mobility $\mathsf{N}(\nabla\mathbf{u}, \mathbf{K}, \nabla\mathbf{K})$, to leading orders in gradients, gives

$$\mathsf{M} = \mathsf{M}_0 + \mathsf{M}_1\nabla\mathbf{u} + m_2\mathbf{K}\mathbf{K} + \mathcal{O}(\nabla\nabla\mathbf{u}) + \mathcal{O}(\nabla\nabla\mathbf{K}), \tag{B1}$$

$$\mathsf{P}\cdot\mathsf{N} = n_1\boldsymbol{\epsilon}\cdot\mathbf{K}\cdot(\boldsymbol{\epsilon}\cdot\nabla\nabla\cdot\mathbf{u}) + n_2\mathsf{P}\cdot\mathbf{K}\nabla\nabla\cdot\mathbf{u} + n_3\mathsf{P}\cdot\nabla\mathbf{K} + \mathcal{O}(\nabla\mathbf{u}\nabla\mathbf{u}) + \mathcal{O}(\nabla\nabla\mathbf{K}). \tag{B2}$$

Here M_0 is the mobility of the undistorted lattice and such a term is not allowed in N due to symmetry under $\mathbf{K}\to-\mathbf{K}$, and $\mathsf{P}\equiv\mathsf{I}-\mathbf{K}\mathbf{K}$ is the projector transverse to the unit vector $\mathbf{K}$. In the first term of Eq. (B2), $\boldsymbol{\epsilon}$ is the Levi-Civita tensor. Retaining only those terms that are allowed by the symmetries leads to the "hydrodynamic" equations for the displacement field $\mathbf{u}$ and orientation field $\mathbf{K}$ in one dimension x by dropping z derivatives Eqs. (3)–(5).

APPENDIX C: WAVE SOLUTIONS FOR SPHEROIDS

The eigenfunctions corresponding to the eigenvalues $(\lambda_1, \lambda_2, \lambda_3) = (0, -i\omega, i\omega)$, where $\omega\equiv\omega_+$ is from Eqs. (17) and (18), are given by $\mathbf{v}_1$, $\mathbf{v}_2$, and $\mathbf{v}_3$, respectively,

$$\mathbf{v}_1 = \begin{pmatrix} 0 \\ -i\dfrac{2d\pi\alpha(e)}{3a}\csc(q) \\ 1 \end{pmatrix}, \quad \mathbf{v}_2 = \begin{pmatrix} i\omega\pi\csc^2\left(\dfrac{q}{2}\right) \\ -\dfrac{1}{2}i\cot\left(\dfrac{q}{2}\right) \\ 1 \end{pmatrix}, \quad \mathbf{v}_3 = \begin{pmatrix} -i\omega\pi\csc^2\left(\dfrac{q}{2}\right) \\ -\dfrac{1}{2}i\cot\left(\dfrac{q}{2}\right) \\ 1 \end{pmatrix}, \tag{C1}$$

giving the solution as a real part,

$$\mathbf{X}(t) = \sum_{i=1}^{3}\frac{a_i}{2}(\mathbf{v_i}e^{iqn}e^{\lambda_i t} + \mathbf{v_i^*}e^{-iqn}e^{\lambda_i^* t}), \tag{C2}$$

where $\mathbf{X}^n = (u_x^n, u_z^n, \delta\theta_q^n)^\intercal$. For $\mathsf{A}\equiv(a_1, a_2, a_3)$, Eq. (C2) becomes $\mathbf{X}^n(t) = \mathbf{B}\cdot\mathsf{A}$, where in the stable regime

$$\mathbf{B} = \begin{pmatrix} 0 & -\omega\pi\csc^2\left(\dfrac{q}{2}\right)\sin(qn-\omega t) & \omega\pi\csc^2\left(\dfrac{q}{2}\right)\sin(qn+\omega t) \\ \dfrac{2d\pi\alpha(e)}{3a}\csc(q)\sin(qn) & \dfrac{1}{2}\cot\left(\dfrac{q}{2}\right)\sin(qn-\omega t) & \dfrac{1}{2}\cot\left(\dfrac{q}{2}\right)\sin(qn+\omega t) \\ \cos(qn) & \cos(qn-\omega t) & \cos(qn+\omega t) \end{pmatrix}. \tag{C3}$$

The coefficients A can be determined from the initial condition, $\mathsf{A} = \mathbf{B}^{-1}\cdot\mathbf{X}^n|_{t=0}$. Our experimental initial condition is $\mathbf{X}^n(t=0) = [\epsilon\sin(qn), 0, 0]^\intercal$, making $\mathsf{A} = \{[\epsilon\sin^2(q/2)]/2\omega\pi\}(0, -1, 1)^\intercal$, which gives the wave solution in the stable regime:

$$u_x^n(t) = \epsilon\sin(qn)\cos(\omega t), \tag{C4}$$

$$u_z^n(t) = \frac{\epsilon\sin(q)}{4\omega\pi}\cos(qn)\sin(\omega t), \tag{C5}$$

$$\delta\theta^n(t) = -\frac{\epsilon\sin^2(q/2)}{\omega\pi}\sin(qn)\sin(\omega t). \tag{C6}$$

Note that the dependence on eccentricity of the spheroids enters through ω from Eqs. (17) and (18). In the unstable regime the eigenvalues $(0, -\lambda, +\lambda)$ are real, giving hyperbolic functions in the time dependence of the solution:

$$u_x^n(t) = \epsilon\sin(qn)\cosh(\lambda t), \tag{C7}$$

$$u_z^n(t) = \frac{\epsilon \sin(q)}{4\lambda\pi}\cos(qn)\sinh(\lambda t), \tag{C8}$$

$$\delta\theta^n(t) = -\frac{\epsilon \sin^2(q/2)}{\lambda\pi}\sin(qn)\sinh(\lambda t). \tag{C9}$$

APPENDIX D: FAR-FIELD SIMULATIONS WITH PERIODIC BOUNDARIES

To understand the nonlinear dynamics of disks in the (x, z) plane, we numerically analyze the equations of motion for spheroids in the limiting case of disks $e \to 1$, to leading order in $\mathcal{O}(a/r)$, by pairwise addition of hydrodynamic interactions using the method of reflections [14]. When lengths are nondimensionalized by a and time by $6\pi\mu a^2/F$, such that velocities are scaled by the settling speed of an isolated sphere, the far-field equations for the positions (x_n, z_n) and orientations θ_n of the nth spheroid become

$$\frac{dx_n}{dt} = \frac{3\pi}{32}\sin 2\theta_n - \sum_{m\neq n}^{N}\frac{3(x_n - x_m)(z_n - z_m)}{4r_{mn}^3}, \tag{D1}$$

$$\frac{dz_n}{dt} = \frac{3\pi}{16}(\sin^2\theta_n - 3) - \sum_{m\neq n}^{N}\frac{3}{4}\left[\frac{1}{r_{mn}} + \frac{(z_n - z_m)^2}{r_{mn}^3}\right], \tag{D2}$$

$$\begin{aligned}\frac{d\theta_n}{dt} = {} & \sum_{m\neq n}^{N}\frac{3(x_n - x_m)}{4r_{mn}^3} \\ & - \sum_{m\neq n}^{N}\frac{9(z_n - z_m)}{4r_{mn}^5}[(x_n - x_m)\cos\theta_n + (z_n - z_m)\sin\theta_n] \\ & \times [(z_n - z_m)\cos\theta_n - (x_n - x_m)\sin\theta_n].\end{aligned} \tag{D3}$$

We numerically solve the above equations using the fourth-order Runge-Kutta method. In the nearest-neighbor approximation, the number of interacting neighbors N truncates the spatial summation over m, making implementation of periodic boundaries straightforward. Equations (D1)–(D3) are for initial conditions in which the orientation vector of all the disks lies in the (x, z) plane and hence the resulting trajectories are confined to the same plane $y = 0$. Although we use Eqs. (D1)–(D3) to investigate lattice configurations, these equations can be used to study the in-plane dynamics of any reference structure. Note that when the interparticle separation r_{mn} between a pair approaches 0, the far-field numerics fails to capture the dynamics. This can be seen in the pair configurations of the form "⊥" (see Video 7 in SM [31]).

[1] G. G. Stokes, *On the Effect of the Internal Friction of Fluids on the Motion of Pendulums*, Trans. Cambridge Philos. Soc. **IX**, 8 (1851).

[2] J. Happel and H. Brenner, *Low Reynolds Number Hydrodynamics: With Special Applications to Particulate Media* (Kluwer Publishers, The Hague, The Netherlands, 1983), Vol. 1.

[3] S. Kim and S. J. Karrila, *Microhydrodynamics: Principles and Selected Applications* (Dover Publications, Mineola, New York, 1991).

[4] J. F. Brady and G. Bossis, *Stokesian Dynamics*, Annu. Rev. Flu. Mech. **20**, 111 (1988).

[5] G. B. Jeffery, *The Motion of Ellipsoidal Particles Immersed in a Viscous Fluid*, Proc. R. Soc. A **102**, 161 (1922).

[6] T. Goldfriend, H. Diamant, and T. A. Witten, *Hydrodynamic Interactions between Two Forced Objects of Arbitrary Shape. I. Effect on Alignment*, Phys. Fluids **27**, 123303 (2015).

[7] T. A. Witten and H. Diamant, *A Review of Shaped Colloidal Particles in Fluids: Anisotropy and Chirality*, arXiv:2003.03698.

[8] A. T. Chwang and T. Y. Wu, *Hydromechanics of Low Reynolds Number Flow, Part 2*, J. Fluid Mech. **67**, 787 (1975).

[9] M. Smoluchowski, *On the Mutual Action of Spheres Which Move in a Viscous Liquid*, Bull. Sci. Cracovie A **1**, 28 (1911).

[10] M. Stimson and G. B. Jeffery, *The Motion of Two Spheres in a Viscous Fluid*, Proc. R. Soc. A **111**, 110 (1926).

[11] E. M. Purcell, *Life at Low Reynolds Number*, Am. J. Phys. **45**, 3 (1977).

[12] S. Jung, S. E. Spagnolie, K. Parikh, M. Shelley, and A. K. Tornberg, *Periodic Sedimentation in a Stokesian Fluid*, Phys. Rev. E **74**, 035302(R) (2006).

[13] S. Wakiya, *Mutual Interaction of Two Spheroids Sedimenting in a Viscous Fluid*, J. Phys. Soc. Jpn. **20**, 1502 (1965).

[14] S. Kim, *Sedimentation of Two Arbitrarily Oriented Spheroids in a Viscous Fluid.*, Int. J. Multiphase Flow **11**, 699 (1985).

[15] R. Chajwa, N. Menon, and S. Ramaswamy, *Kepler Orbits in Pairs of Disks Settling in a Viscous Fluid*, Phys. Rev. Lett. **122**, 224501 (2019).

[16] S. Ramaswamy, *Issues in the Statistical Mechanics of Steady Sedimentation*, Adv. Phys. **50**, 297 (2001).

[17] A. J. C Ladd and R. Verberg, *Lattice-Boltzmann Simulations of Particle-Fluid Suspensions*, J. Stat. Phys. **104**, 1191 (2001).

[18] S.-Y. Tee, P. J. Mucha, L. Cipelletti, S. Manley, M. P. Brenner, P. N. Segre, and D. A. Weitz, *Nonuniversal Velocity Fluctuations of Sedimenting Particles*, Phys. Rev. Lett. **89**, 054501 (2002).

[19] É. Guazzelli and J. Hinch, *Fluctuations and Instability in Sedimentation*, Annu. Rev. Fluid Mech. **43**, 97 (2011).

[20] D. L. Koch and E. S. G. Shaqfeh, *The Instability of a Dispersion of Sedimenting Spheroids*, J. Fluid Mech. **209**, 521 (1989).

[21] B. Metzger, J. E. Butler, and E. Guazzelli, *Experimental Investigation of the Instability of a Sedimenting Suspension of Fibres*, J. Fluid Mech. **575**, 307 (2007).

[22] K. Gustavsson and A.-K. Tornberg, *Gravity Induced Sedimentation of Slender Fibers*, Phys. Fluids **21**, 123301 (2009).

[23] T. Goldfriend, H. Diamant, and T. A. Witten, *Screening, Hyperuniformity, and Instability in the Sedimentation of Irregular Objects*, Phys. Rev. Lett. **118**, 158005 (2017).

[24] A. A. Zick and G. M. Homsy, *Stokes Flow through Periodic Arrays of Spheres*, J. Fluid Mech. **115**, 13 (1982).

[25] J. M. Crowley, *Viscosity-Induced Instability of a One-Dimensional Lattice of Falling Spheres.*, J. Fluid Mech. **45**, 151 (1971).

[26] J. M. Crowley, *Clumping Instability of a Falling Horizontal Lattice*, Phys. Fluids **19**, 1296 (1976).

[27] P. Chaikin, *Thermodynamics and Hydrodynamics of Hard Spheres: The Role of Gravity, Soft and Fragile Matter*, *Soft and Fragile Matter: Nonequilibrium Dynamics, Metastability and Flow*, edited by M. E. Cates and M. R. Evans, Scottish Graduate Textbook Series (CRC Press, Boca Raton, FL, 2000), pp. 315–348.

[28] R. Lahiri and S. Ramaswamy, *Are Steadily Moving Crystals Unstable?*, Phys. Rev. Lett. **79**, 1150 (1997).

[29] R. Lahiri, M. Barma, and S. Ramaswamy, *Strong Phase Separation in a Model of Sedimenting Lattices*, Phys. Rev. E **61**, 1648 (2000).

[30] R. A. Simha and S. Ramaswamy, *Traveling Waves in a Drifting Flux Lattice*, Phys. Rev. Lett. **83**, 3285 (1999).

[31] See Supplemental Material at http://link.aps.org/supplemental/10.1103/PhysRevX.10.041016 for Videos 1–7.

[32] B. Farrell, *Modal and Nonmodal Baroclinic Waves*, J. Atmos. Sci. **41**, 668 (1984).

[33] P. J. Schmid, *Nonmodal Stability Theory*, Annu. Rev. Fluid Mech. **39**, 129 (2007).

[34] R. Bale and R. Govindarajan, *Transient Growth and Why We Should Care About It*, Resonance **15**, 441 (2010).

[35] L. N. Trefethen, A. E. Trefethen, S. C. Reddy, and T. A. Driscoll, *Hydrodynamic Stability without Eigenvalues*, Science **261**, 578 (1993).

[36] A. Zöttl and H. Stark, *Nonlinear Dynamics of a Microswimmer in Poiseuille Flow*, Phys. Rev. Lett. **108**, 218104 (2012).

[37] H. Stark, *Swimming in External Fields*, Eur. Phys. J. Special Topics **225**, 2369 (2016).

[38] A. Bolitho, R. Singh, and R. Adhikari, *Periodic Orbits of Active Particles Induced by Hydrodynamic Monopoles*, Phys. Rev. Lett. **124**, 088003 (2020).

[39] E. Lushi and P. M. Vlahovska, *Periodic and Chaotic Orbits of Plane-Confined Micro-rotors in Creeping Flows*, J. Nonlinear Sci. **25**, 1111 (2015).

[40] N. Oppenheimer, D. B. Stein, and M. J. Shelley, *Rotating Membrane Inclusions Crystallize through Hydrodynamic and Steric Interactions*, Phys. Rev. Lett. **123**, 148101 (2019).

[41] P. C. Martin, O. Parodi, and P. S. Pershan, *Unified Hydrodynamic Theory for Crystals, Liquid Crystals, and Normal Fluids*, Phys. Rev. A **6**, 2401 (1972).

[42] M. M. M. El Telbany and A. J. Reynolds, *The Structure of Turbulent Plane Couette Flow*, J. Fluid Eng. **104**, 367 (1982).

[43] M. L. Ekiel-Jeżewskaa and E. Wajnryb, *Hydrodynamic Orienting of Asymmetric Microobjects Under Gravity*, J. Phys. Condens. Matter **21**, 204102 (2009).

[44] A. Conway *et al.*, *Sedimentation of Polygonal Tiles*, Bull. Am. Phys. Soc. **64**, G23.00007 (2019), https://meetings.aps.org/Meeting/DFD19/Session/G23.7.

[45] N. W. Krapf, T. A. Witten, and N. C. Keim, *Chiral Sedimentation of Extended Objects in Viscous Media*, Phys. Rev. E **79**, 056307 (2009).

[46] T. A. Witten and H. Diamant, *A Review of Shaped Colloidal Particles in Fluids: Anisotropy and Chirality*, arXiv:2003.03698.

[47] C. E. Marshall, *Studies in the Degree of Dispersion of the Clays. IV. The Shapes of Clay Particles*, J. Phys. Chem. **45**, 81 (1941).

[48] W. T. Hung, A. F. Collings, and J. Low, *Erythrocyte Sedimentation Rate Studies in Whole Human Blood*, Phys. Med. Biol. **39**, 1855 (1994).